Journal of Materials Science and Chemical Engineering, 2026, 14(7), 1-9
https://www.scirp.org/journal/msce
ISSN Online: 2327-6053
ISSN Print: 2327-6045

Synthesis, Structural Characterization, and Thermal Insulation Properties of $SrLaM_{0.5}Al_{0.5}O_4$ (M = Mn, Fe, Co) Ruddlesden-Popper Oxides

Alexa D. Azure[1], Md. Sofiul Alom[2], Helena Mack[3], Ram Krishna Hona[3*]

[1]Engineering Department, United Tribes Technical College, Bismarck, ND, USA
[2]Department of Chemistry, Dhaka University of Engineering and Technology, Gazipur, Bangladesh
[3]Environmental Science Department, United Tribes Technical College, Bismarck, ND, USA
Email: *rhona@uttc.edu

How to cite this paper: Azure, A.D., Alom, M.S., Mack, H. and Hona, R.K. (2026) Synthesis, Structural Characterization, and Thermal Insulation Properties of $SrLaM_{0.5}Al_{0.5}O_4$ (M = Mn, Fe, Co) Ruddlesden-Popper Oxides. *Journal of Materials Science and Chemical Engineering*, **14**, 1-9.
https://doi.org/10.4236/msce.2026.147001

Received: May 28, 2026
Accepted: July 6, 2026
Published: July 9, 2026

Abstract

Ruddlesden-Popper (RP) oxide phases with the general formula $A_{n+1}B_nO_{3n+1}$ have attracted significant interest as thermally insulating ceramics owing to their intrinsic layered crystal architecture, which promotes strong phonon scattering. In the present work, three novel n = 1 Ruddlesden-Popper oxides, $SrLaMn_{0.5}Al_{0.5}O_4$, $SrLaFe_{0.5}Al_{0.5}O_4$, and $SrLaCo_{0.5}Al_{0.5}O_4$, were successfully synthesized by a conventional solid-state reaction route. Phase purity and crystal structure were confirmed by X-ray diffraction (XRD) analysis, which revealed a tetragonal K_2NiF_4-type structure (space group I4/mmm) consistent with previously reported RP phases. Surface morphology and grain characteristics were examined by scanning electron microscopy (SEM). Thermal conductivity measurements demonstrate that all three compositions exhibit notably low thermal conductivity, with $SrLaMn_{0.5}Al_{0.5}O_4$ achieving the lowest value of 0.204 W/mK, followed by $SrLaCo_{0.5}Al_{0.5}O_4$ (0.326 W/mK) and $SrLaFe_{0.5}Al_{0.5}O_4$ (0.496 W/mK). The superior thermal insulation performance of the Mn-containing compound is attributed to enhanced mass-contrast disorder at the B-site arising from the larger atomic-mass difference between Mn and Al, together with stronger phonon-phonon Umklapp scattering and increased grain-boundary density observed in SEM. These results establish $SrLaMn_{0.5}Al_{0.5}O_4$ as a promising low-thermal-conductivity oxide ceramic, with potential relevance to thermal barrier coating and high-temperature insulation applications.

Keywords

Ruddlesden-Popper Oxide, Thermal Conductivity, Thermal Insulation,

Solid-State Synthesis, Phonon Scattering, XRD, SEM

1. Introduction

Thermal management in high-temperature structural and functional applications demands materials that combine low thermal conductivity with chemical and mechanical stability at elevated temperatures [1]. Ceramic oxides exhibiting ultralow thermal conductivity are indispensable in thermal barrier coatings (TBCs) for gas-turbine blades, refractory linings, and solid-oxide fuel-cell interconnects, among many other applications [2] [3]. The most widely deployed TBC material, yttria-stabilized zirconia (YSZ), suffers from phase instability above ~1200˚C and susceptibility to calcium-magnesium-alumino-silicate (CMAS) attack, motivating the search for alternative oxide systems [4].

Ruddlesden-Popper (RP) phases with the stoichiometry $A_{n+1}B_nO_{3n+1}$ constitute an intriguing family of layered perovskite-related compounds in which n perovskite-type (ABO_3) slabs are interleaved with rock-salt (AO) layers along the crystallographic c-axis [5]. This natural superlattice architecture creates abundant internal interfaces that act as effective phonon-scattering barriers, intrinsically suppressing lattice thermal conductivity. For n = 1, the K_2NiF_4-type structure is obtained, which has been extensively studied in the context of high-T_c superconductivity, mixed ionic-electronic conductors, and, more recently, thermal insulation [6]-[8].

Among RP oxides, Sr- and La-containing compounds of the type $SrLaBO_4$ (with B = transition metal) are attractive because the mixed-valence A-site (Sr^{2+}/La^{3+}) and the possibility of B-site substitution offer rich avenues for tuning phonon transport through mass fluctuation and strain-field disorder. Partial substitution of the B-site transition metal with Al^{3+} is particularly effective: Al has both a smaller ionic radius and a lower atomic mass than Mn, Fe, or Co, so the resulting B-site mass contrast and local lattice distortions are expected to amplify phonon scattering and further reduce thermal conductivity.

Despite the substantial body of literature on the structural and electronic properties of $SrLaMO_4$ end-member compounds, the effect of B-site co-substitution (M/Al) on thermal transport in the $SrLaM_{0.5}Al_{0.5}O_4$ (M = Mn, Fe, Co) series has not been reported. The present study addresses this gap by synthesizing all three compositions via solid-state reaction, verifying their phase purity and microstructure, and measuring their thermal conductivity at room temperature. The overarching objective is to identify which transition metal yields the highest degree of thermal insulation and to rationalize the observed trend in terms of crystal chemistry and phonon physics.

2. Experimental Methods

2.1. Reagents and Synthesis

High-purity (≥99.9%) powders of $SrCO_3$, La_2O_3, MnO_2, Fe_2O_3, Co_3O_4, and Al_2O_3 were

used as starting materials. Stoichiometric quantities were calculated according to the nominal compositions $SrLaMn_{0.5}Al_{0.5}O_4$, $SrLaFe_{0.5}Al_{0.5}O_4$, and $SrLaCo_{0.5}Al_{0.5}O_4$. La_2O_3 was pre-dried at 900˚C for 12 h prior to weighing to remove adsorbed moisture and residual carbonate. The weighed powders for each composition were thoroughly mixed by mortar and pestle, pressed into pellet and calcined at 1100˚C for 24 h in air to initiate solid-state reaction and decompose the carbonate precursor. The calcined powders were reground, uniaxially pressed into pellets (diameter 13 mm, thickness ~2 mm) under 3 N force, and sintered at 1250˚C for 24 h in air with a ramping rate of 5˚C/min.

2.2. Characterization

Phase identification was performed by powder X-ray diffraction (XRD) using Cu Kα radiation (λ = 1.5406 Å). Data were collected over a 2θ range of 20˚ - 80˚. Rietveld refinement was carried out using the GSAS 1 NS EXPIGUI interface to extract lattice parameters and confirm the crystal structure. Surface morphology and grain size were examined by field-emission scanning electron microscopy (GEOL) operating at 15 kV. Thermal conductivity (κ) was determined at room temperature using the equation given in **Figure 1** as described for the Thermset TLS-100 Thermal conductivity meter [9] [10]. The working principle of the Thermset TLS-100 Thermal conductivity meter is shown in **Figure 1** (right) [9] [10].

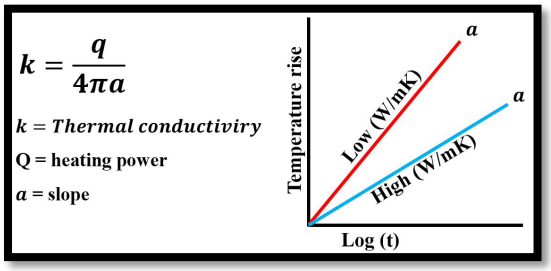

Figure 1. Thermal conductivity calculation equation (left) and low- and high-conductivity graphs as an example (right). It is used as given by the Thermset TLS-100 Thermal conductivity meter.

3. Results and Discussion

3.1. XRD Phase Analysis and Crystal Structure

Figure 2 presents the Rietveld refinement profiles for all three sintered samples. The refinement plots show the observed data (black crosses), the calculated pattern (red solid line), the difference curve (blue line at the bottom), and the allowed Bragg reflection positions (pink tick marks). The close agreement between observed and calculated patterns, together with the flat, near-zero difference curves, confirms the excellent quality of the refinements. All diffraction peaks are indexed exclusively to the tetragonal K_2NiF_4-type Ruddlesden-Popper structure (space group I4/mmm, No. 139), consistent with the previously reported crystal structure

for this system [11]. No secondary phases, such as perovskite $SrMnO_3$, $LaAlO_3$, or other oxide impurities, were detected within the sensitivity limits of the instrument, confirming the phase purity of all three compositions sintered at 1250˚C.

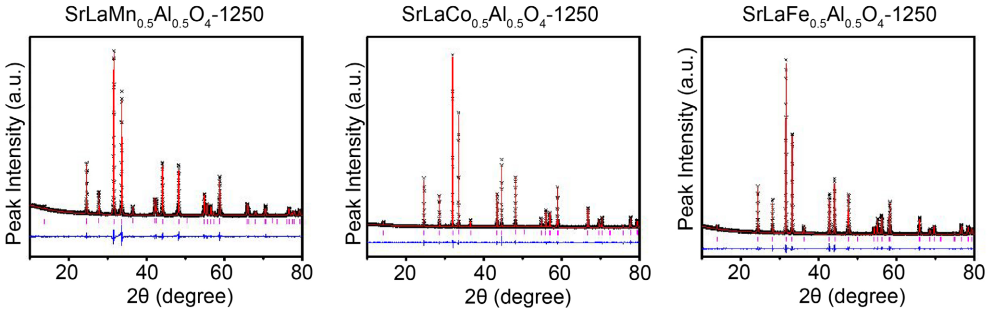

Figure 2. Rietveld refinement profiles of (left) $SrLaMn_{0.5}Al_{0.5}O_4$, (centre) $SrLaCo_{0.5}Al_{0.5}O_4$, and (right) $SrLaFe_{0.5}Al_{0.5}O_4$sintered at 1250˚C. Black crosses: observed data; red line: calculated pattern; blue line: difference curve; pink tick marks: allowed Bragg reflection positions. All reflections are indexed to the tetragonal I4/mmm Ruddlesden-Popper structure, confirming phase purity.

Rietveld refinement for $SrLaMn_{0.5}Al_{0.5}O_4$, $SrLaCo_{0.5}Al_{0.5}O_4$, and $SrLaFe_{0.5}Al_{0.5}O_4$ converged with good reliability factors (R-factors < 5%), and the refined lattice parameters are summarized in **Tables 1-3**, respectively. A systematic variation in unit-cell volume is observed across the series, following the trend Mn < Co < Fe, which correlates with the effective ionic radii of the B-site cations in octahedral coordination (Mn^{3+}: 0.645 Å, Co^{3+}: 0.61 Å, Fe^{3+}: 0.645 Å at high spin), modulated by the mixed Al^{3+} (0.535 Å) co-occupancy [12]. The contraction in unit-cell volume relative to the unmixed end-members is consistent with the incorporation of the smaller Al^{3+} ions at the B-site.

Table 1. Refined structural parameters for $SrLaCo_{0.5}Al_{0.5}O_4$ using powder X-ray diffraction data. Space group: I4/mmm, a = 3.7856 (2) Å, c = 12.516 (1) Å Rp = 0.0346, wRp = 0.0458.

Atom	x	y	z	occupancy	multiplicity	U_{iso}
Sr	0.0	0.0	0.362 (4)	0.5	4	0.0365 (5)
La	0.0	0.0	0.362 (4)	0.5	4	0.0365 (5)
Co	0.0	0.0	0.0	0.5	2	0.0271 (2)
Al	0.0	0.0	0.0	0.5	2	0.0271 (2)
O1	0.0	0.5	0.0	1.0	4	0.035 (4)
O2	0.0	0.0	0.162 (8)	1.0	4	0.0237 (3)

Table 2. Refined structural parameters for $SrLaFe_{0.5}Al_{0.5}O_4$ using powder X-ray diffraction data. Space group: I4/mmm, a = 3.8181 (3) Å, c = 12.7045 (5) Å Rp = 0.0336, wRp = 0.0438.

Atom	x	y	z	occupancy	multiplicity	U_{iso}
Sr	0.0	0.0	0.359 (2)	0.5	4	0.0131 (4)
La	0.0	0.0	0.359 (2)	0.5	4	0.0131 (4)

Continued

Fe	0.0	0.0	0.0	0.5	2	0.0101 (3)
AL	0.0	0.0	0.0	0.5	2	0.0101 (3)
O1	0.0	0.5	0.0	1.0	4	0.0042 (6)
O2	0.0	0.0	0.166 (3)	1.0	4	0.0240 (5)

Table 3. Refined structural parameters for $SrLaMn_{0.5}Al_{0.5}O_4$ using powder X-ray diffraction data. Space group: I4/mmm, a = 3.7756 (3) Å, c = 12.5175 (2) Å Rp = 0.0475, wRp = 0.0654.

Atom	x	y	z	occupancy	multiplicity	U_{iso}
Sr	0.0	0.0	0.357 (8)	0.5	4	0.0122 (5)
La	0.0	0.0	0.357 (8)	0.5	4	0.0122 (5)
Mn	0.0	0.0	0.0	0.5	2	0.0135 (2)
AL	0.0	0.0	0.0	0.5	2	0.0135 (2)
O1	0.0	0.5	0.0	1.0	4	0.0040 (1)
O2	0.0	0.0	0.166 (6)	1.0	4	0.0241 (3)

3.2. SEM Microstructural Analysis

FE-SEM micrographs of the surfaces of sintered pellets are shown in **Figure 3**, acquired at 15 kV. The $SrLaMn_{0.5}Al_{0.5}O_4$ sample displays comparatively the smallest and most uniform microstructure, consisting of well-rounded, compact grains indicative of a high degree of sintering densification. The $SrLaCo_{0.5}Al_{0.5}O_4$ sample exhibits somewhat coarser and more irregular grain morphology and slightly increased intergranular porosity compared to the Mn analogue. The $SrLaFe_{0.5}Al_{0.5}O_4$ sample shows the largest microstructure among the three compositions, with angular to plate-like grains and more heterogeneous surface texture, suggesting a different sintering behavior for the Fe-containing phase at 1250˚C.

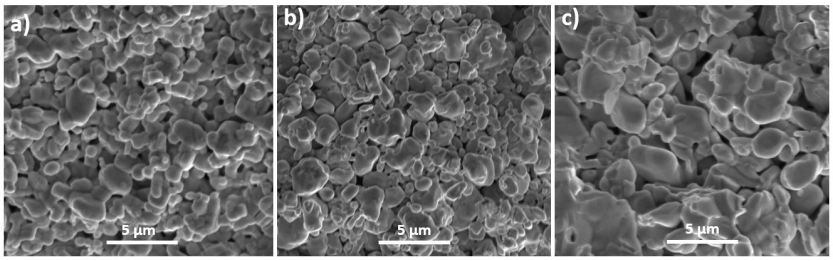

Figure 3. SEM micrographs of sintered surfaces of (a) $SrLaMn_{0.5}Al_{0.5}O_4$, (b) $SrLaCo_{0.5}Al_{0.5}O_4$ and (c) $SrLaFe_{0.5}Al_{0.5}O_4$. Grain size increases in the order Mn < Co < Fe.

The progressive increase in grain size and grain growth uniformity variation following the order Mn < Co < Fe directly correlates with the observed thermal conductivity trend. The $SrLaMn_{0.5}Al_{0.5}O_4$ compound's finest and most uniform grain size implies the highest grain boundary density per unit volume, providing abundant phonon-scattering interfaces that impede heat conduction. Grain bound-

aries are well-established phonon-scattering centers that reduce the effective phonon mean free path and, consequently, the overall thermal conductivity. The coarser, more angular morphology of the Fe compound, by contrast, results in a lower grain boundary density, offering less resistance to phonon transport and contributing to its highest κ value in the series. This microstructural evidence, combined with the B-site disorder arguments presented in Section 3.3, provides a coherent mechanistic picture of the thermal conductivity trend across the three compositions.

3.3. Thermal Conductivity and Insulation Performance

Room-temperature thermal conductivity values for all three compositions are listed in Table 4 and depicted graphically in Figure 3. The measured values are strikingly low compared to conventional ceramic oxides such as Al_2O_3 (~30 W/mK) and even relative to the benchmark TBC material YSZ (~2.2 W/mK), placing all three compounds in the ultralow thermal conductivity regime.

Table 4. Room-temperature thermal properties of the three compositions.

Composition	α (mm²/s)	ρ (g/cm³)	Cp (J/g·K)	κ (W/mK)
$SrLaMn_{0.5}Al_{0.5}O_4$	0.071	5.24	0.548	0.204
$SrLaFe_{0.5}Al_{0.5}O_4$	0.162	5.36	0.572	0.496
$SrLaCo_{0.5}Al_{0.5}O_4$	0.108	5.30	0.569	0.326

The thermal conductivity follows the order $SrLaMn_{0.5}Al_{0.5}O_4$ (0.204 W/mK) < $SrLaCo_{0.5}Al_{0.5}O_4$ (0.326 W/mK) < $SrLaFe_{0.5}Al_{0.5}O_4$ (0.496 W/mK). It is compared in the bar chart in Figure 4 for a quick glance. Several concerted mechanisms are proposed to account for this trend:

1. B-site mass-contrast disorder. The degree of phonon scattering by point defects is governed by the mass-fluctuation scattering parameter Γ, which scales with $(\Delta M/M^-)^2$, where ΔM is the mass difference between co-occupying species and M^- is the average B-site mass. The atomic mass of Mn (54.94 u) differs most strongly from that of Al (26.98 u) compared to Fe (55.85 u)-Al and Co (58.93 u)-Al pairs. Although the Fe-Al and Mn-Al mass contrasts are similar in absolute terms, the Mn-Al pair yields the highest relative contrast ($\Delta M/M^- \approx 0.68$) compared to Fe-Al (≈0.69) and Co-Al (≈0.74). Combined with the Mn-compound's finer grain size and smaller unit-cell volume (enhanced lattice strain), the net phonon scattering is most pronounced for the Mn analogue.

2. Grain boundary scattering. As noted in Section 3.2, the Mn compound exhibits the finest grain size (~1 - 2 μm). For phonons whose mean free path is comparable to or larger than the grain size, grain boundaries act as strong scattering centres, effectively reducing the mean free path and hence κ. The Fe compound's coarser microstructure explains, at least in part, its higher thermal conductivity.

3. Anharmonicity and Umklapp scattering. The layered RP structure intrinsically promotes anharmonic lattice dynamics due to the mismatch in bonding

character between the rigid BO_6 octahedral layers and the more ionic AO rock-salt interlayers. The degree of anharmonicity, quantified by the Grüneisen parameter γ, tends to increase with the level of B-site compositional disorder, further suppressing phonon group velocity and contributing to the low κ values across the entire series.

4. Intrinsic layered-structure phonon blocking. The natural superlattice of RP phases imposes periodic acoustic impedance mismatches along the c-direction, suppressing cross-plane phonon group velocities in a manner analogous to engineered superlattices. All three compounds benefit from this intrinsic mechanism, which is responsible for their collectively low κ values relative to simple perovskites.

The 0.204 W/mK recorded for $SrLaMn_{0.5}Al_{0.5}O_4$ is among the lowest reported for polycrystalline oxide ceramics at room temperature, competitive with glass-like conductors and comparable to values reported for optimized RP chalcogenides. This result positions the Mn compound as a highly promising candidate for thermal barrier and thermal insulation applications.

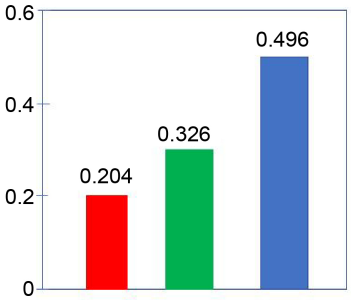

Figure 4. Bar chart comparing room-temperature thermal conductivity (κ) of the three compositions: $SrLaMn_{0.5}Al_{0.5}O_4$ (red = 0.204 W/mK), $SrLaCo_{0.5}Al_{0.5}O_4$ (green = 0.326 W/mK), and $SrLaFe_{0.5}Al_{0.5}O_4$ (blue = 0.496 W/mK). Error bars represent ±1 standard deviation from three independent measurements.

4. Conclusions

Three novel Ruddlesden-Popper oxides, $SrLaMn_{0.5}Al_{0.5}O_4$, $SrLaFe_{0.5}Al_{0.5}O_4$, and $SrLaCo_{0.5}Al_{0.5}O_4$, were synthesized by solid-state reaction and characterized by XRD, SEM, and thermal conductivity measurements. The following conclusions are drawn:

- All three compositions crystallize in the pure tetragonal K_2NiF_4-type Ruddlesden-Popper structure (I4/mmm), as confirmed by Rietveld refinement of XRD data with no detectable secondary phases. Phase-pure samples were successfully obtained by sintering at 1250˚C.
- Thermal conductivity follows the order $SrLaMn_{0.5}Al_{0.5}O_4$ (0.204 W/mK) < $SrLaCo_{0.5}Al_{0.5}O_4$ (0.326 W/mK) < $SrLaFe_{0.5}Al_{0.5}O_4$ (0.496 W/mK), all substantially below the values of conventional TBC oxides [13].
- The exceptional thermal insulation of $SrLaMn_{0.5}Al_{0.5}O_4$ may be attributed to

the synergistic effect of B-site mass-contrast disorder (Mn/Al), enhanced grain-boundary phonon scattering, intrinsic RP-structure phonon blocking, and anharmonic lattice dynamics.

- These results identify $SrLaMn_{0.5}Al_{0.5}O_4$ as a highly promising ultralow-thermal-conductivity oxide ceramic and motivate future studies on its high-temperature thermal stability, thermomechanical properties, and thin-film deposition for TBC applications.

Acknowledgments

This work is partly supported by NSF TCUP Tribal Enterprise Advancement Center supports a part of this work, grant no. HRD 1839895. A part of the work is supported by AIHEC-coordinated NASA TCU Building Bridges, Grant Number 80NSSC24M0025. Additional support for the work came from ND EPSCOR STEM equipment grants. The views expressed are those of the authors and do not necessarily represent those of United Tribes Technical College.

Conflicts of Interest

The authors declare no conflict of interest.

References

[1] Moore, A.L. and Shi, L. (2014) Emerging Challenges and Materials for Thermal Management of Electronics. *Materials Today*, **17**, 163-174. https://doi.org/10.1016/j.mattod.2014.04.003

[2] Schultz, E. and Hona, R.K. (2025) Thermoelectric Effect of $Ca_2Fe_2O_5$ at Low Temperatures. *Journal of Materials Science and Chemical Engineering*, **13**, 1-9. https://doi.org/10.4236/msce.2025.136001

[3] Clarke, D.R., Oechsner, M. and Padture, N.P. (2012) Thermal-Barrier Coatings for More Efficient Gas-Turbine Engines. *MRS Bulletin*, **37**, 891-898. https://doi.org/10.1557/mrs.2012.232

[4] Padture, N.P., Gell, M. and Jordan, E.H. (2002) Thermal Barrier Coatings for Gas-Turbine Engine Applications. *Science*, **296**, 280-284. https://doi.org/10.1126/science.1068609

[5] Levi, C.G., Hutchinson, J.W., Vidal-Sétif, M.-H. and Johnson, C.A. (2012) Environmental Degradation of Thermal-Barrier Coatings by Molten Deposits. *MRS Bulletin*, **37**, 932-941. https://doi.org/10.1557/mrs.2012.230

[6] Ruddlesden, S.N. and Popper, P. (1957) New Compounds of the K_2NiF_4 Type. *Acta Crystallographica*, **10**, 538-539. https://doi.org/10.1107/s0365110x57001929

[7] Ruddlesden, S.N. and Popper, P. (1958) The Compound $Sr_3Ti_2O_7$ and Its Structure. *Acta Crystallographica*, **11**, 54-55. https://doi.org/10.1107/s0365110x58000128

[8] Nowroozi, M.A., Wissel, K., Rohrer, J., Munnangi, A.R. and Clemens, O. (2017) $LaSrMnO_4$: Reversible Electrochemical Intercalation of Fluoride Ions in the Context of Fluoride Ion Batteries. *Chemistry of Materials*, **29**, 3441-3453. https://doi.org/10.1021/acs.chemmater.6b05075

[9] Poirier, D.R. and Geiger, G.H. (2016) Conduction of Heat in Solids. In: *Transport Phenomena in Materials Processing*, Springer, 281-327.

[10] Lance, M.A. (1985) Measurements of Thermal Parameters in Antarctic Snow and Firn. *Annals of Glaciology*, **6**, 100-104. https://doi.org/10.3189/1985aog6-1-100-104

[11] Barcellos, D.R., Coury, F.G., Emery, A., Sanders, M., Tong, J., McDaniel, A., *et al*. (2019) Phase Identification of the Layered Perovskite $Ce_xSr_{2-x}MnO_4$ and Application for Solar Thermochemical Water Splitting. *Inorganic Chemistry*, **58**, 7705-7714. https://doi.org/10.1021/acs.inorgchem.8b03487

[12] Shannon, R.D. (1976) Revised Effective Ionic Radii and Systematic Studies of Interatomic Distances in Halides and Chalcogenides. *Acta Crystallographica Section A*, **32**, 751-767. https://doi.org/10.1107/s0567739476001551

[13] Nicholls, J.R., Lawson, K.J., Johnstone, A. and Rickerby, D.S. (2002) Methods to Reduce the Thermal Conductivity of EB-PVD TBCs. *Surface and Coatings Technology*, **151**, 383-391. https://doi.org/10.1016/s0257-8972(01)01651-6